Supporting information

Large size $BiVO_4$ photoanode with high-stability for efficient water oxidation and wastewater treatment coupled with H_2 evolution

Yan Yang[a], Shipeng Wan [ab]*, Si Li[a], Ruonan Wang[a], Man Ou[c], Biming Liu[d], Qin Zhong[a]*

[a]*School of Chemical Engineering, Nanjing University of Science and Technology, Nanjing, Jiangsu 210094, PR China*

[b]*Department of Chemical and Biomolecular Engineering, Yonsei University, 50 Yonsei-ro, Seodaemun-gu, Seoul 120-749, Republic of Korea*

[c]*School of Energy Science and Engineering, Nanjing University of Technology, Nanjing, Jiangsu 211816, PR China*

[d]*School of Environment, Tsinghua University, Beijing, 100084, PR China*

**Corresponding author*

Email Address: wansp0311@163.com (S. Wan); zq304@njust.edu.cn. (Q. Zhong)

Supplementary figures and discussions

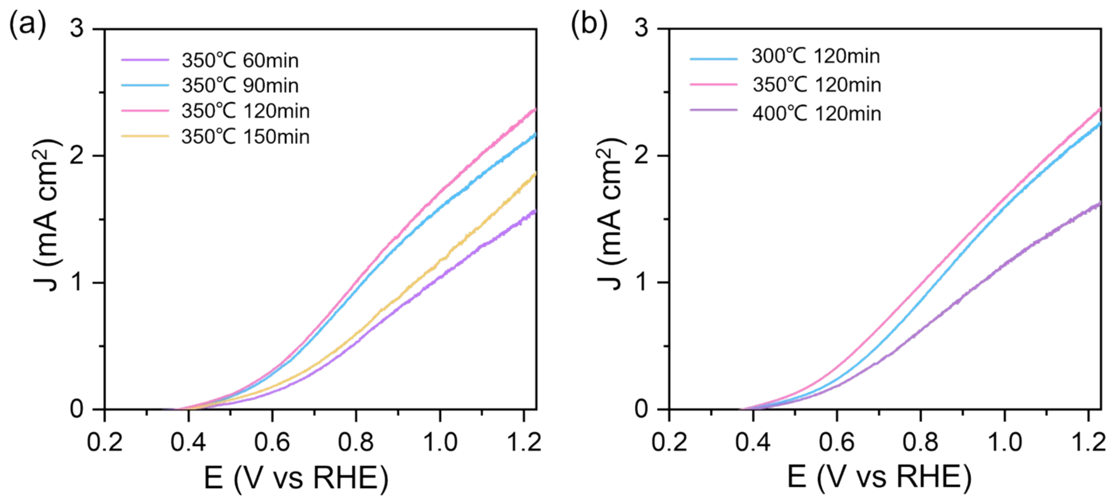

Fig. S1. (a) LSV curves of mixed gas of NH_3 and N_2 annealed $BiVO_4$ photoanode at various time and (b) various temperatures.

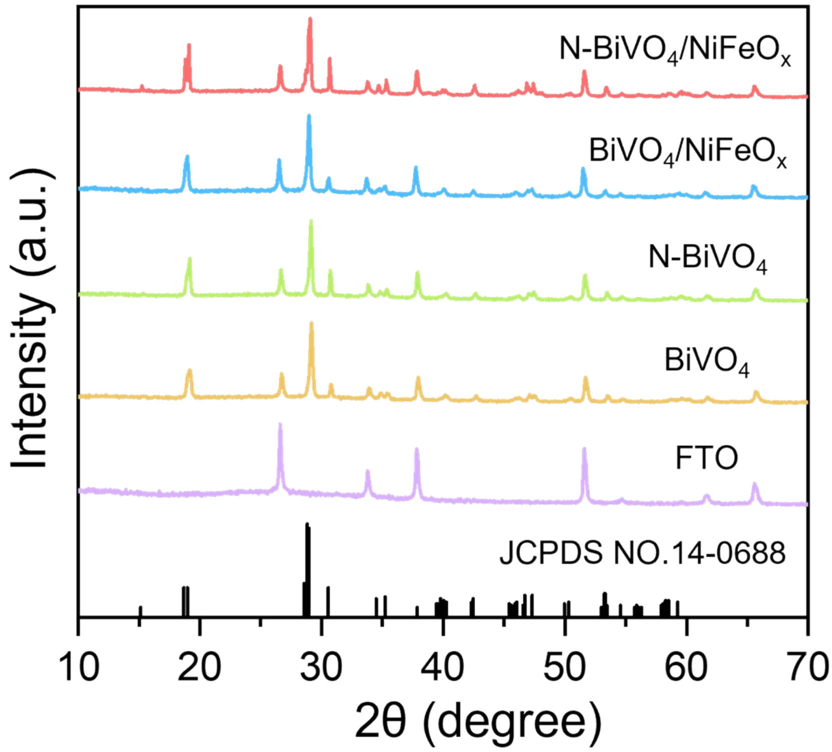

Fig. S2. XRD pattern of fluorine-doped SnO_2 (FTO), $BiVO_4$, N-$BiVO_4$, $BiVO_4$/$NiFeO_x$, N-$BiVO_4$/$NiFeO_x$.

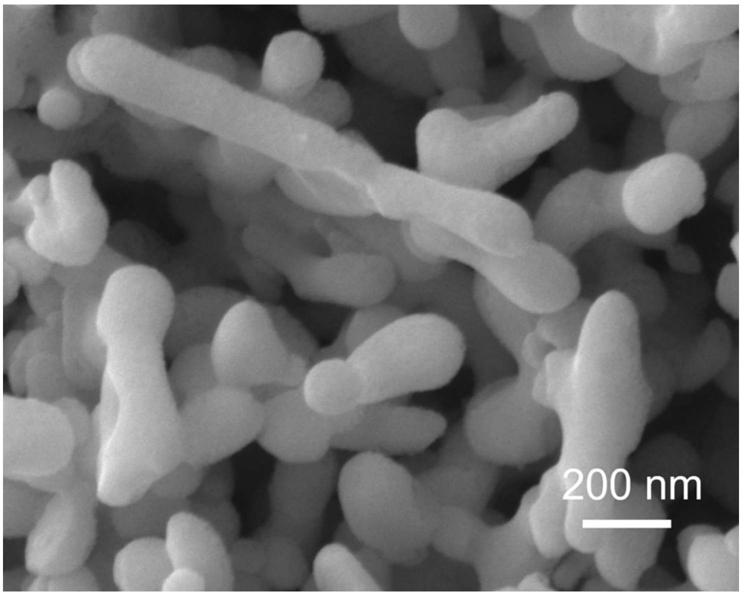

Fig. S3. SEM image of the top view of $BiVO_4$.

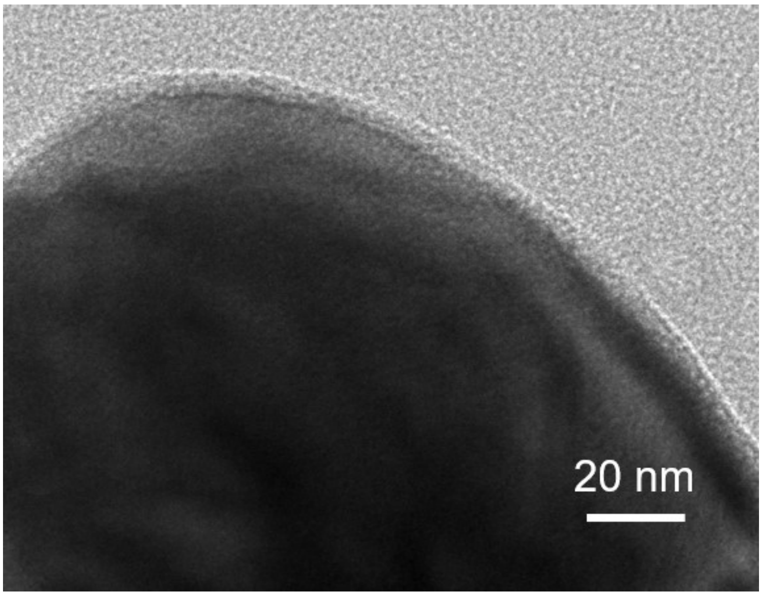

Fig. S4. TEM images of N-$BiVO_4$/$NiFeO_x$.

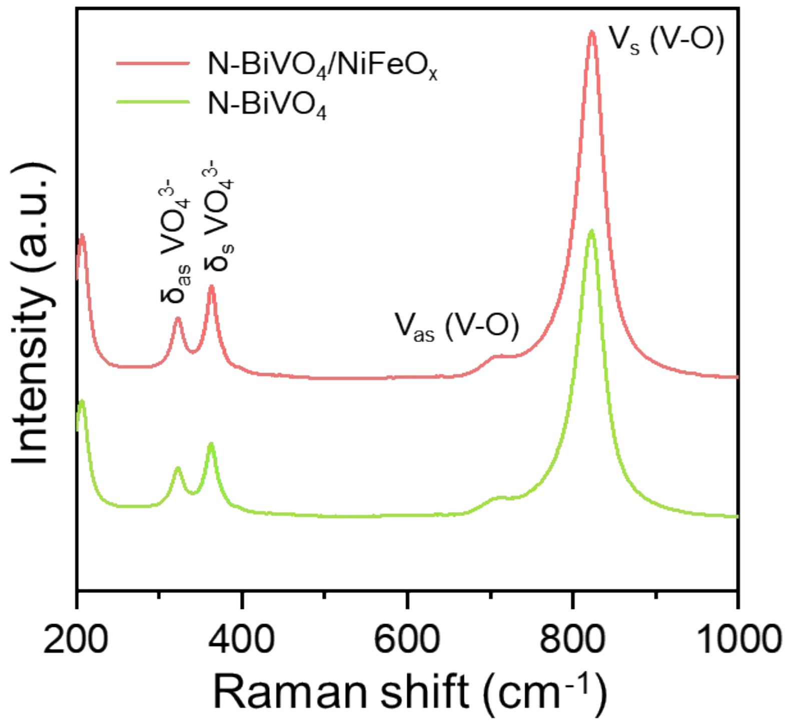

Fig. S5. Raman spectra of N-$BiVO_4$ and N-$BiVO_4$/$NiFeO_x$ photoanodes.

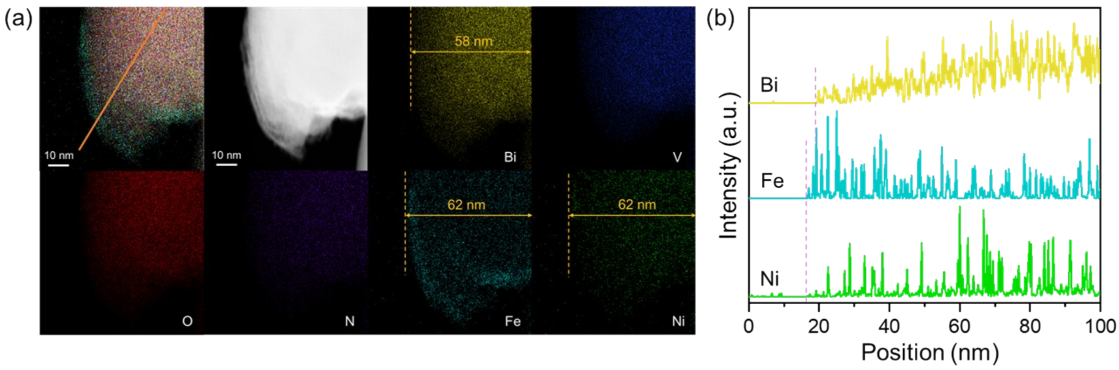

Fig. S6. TEM-EDS (a) elemental mapping (b) and line scanning analysis for N-$BiVO_4$/$NiFeO_x$ photoanodes.

As shown in Fig. S5a, the dimensions Bi, Fe and Ni element distributions in the TEM-EDS mapping have been precisely measured, demonstrating larger distribution of Fe and Ni element (62 nm) than Bi element (58 nm). In addition, from line-scan image (Fig. S5b), before the appearance of Bi element, obvious Fe and Ni signal has been detected in the line-scan profiles. Base-on the above analysis, it can be confirmed that the surface layer on N-$BiVO_4$ crystal was $NiFeO_x$.

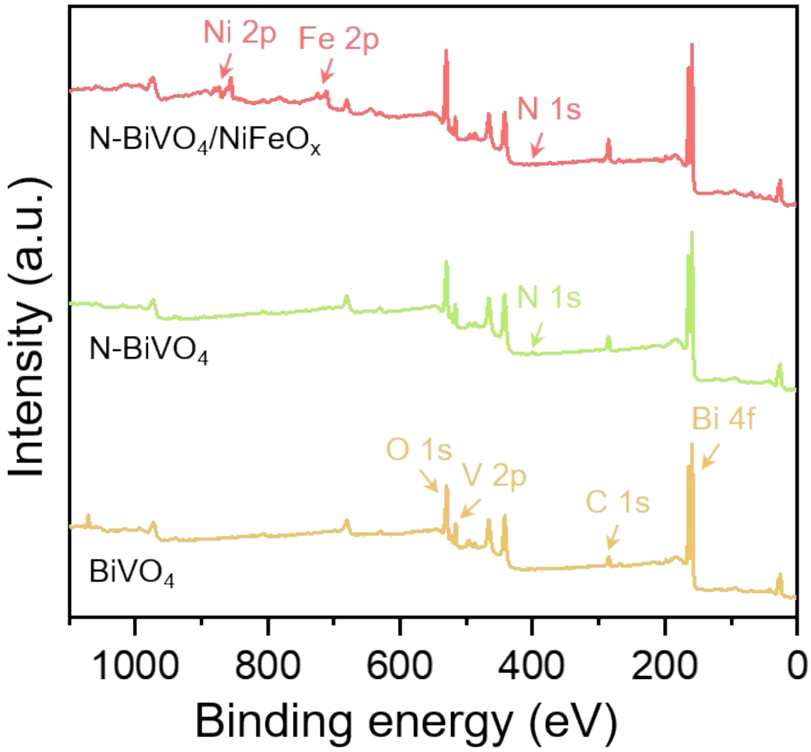

Fig. S7. XPS survey scan spectra of $BiVO_4$, N-$BiVO_4$ and N-$BiVO_4$/$NiFeO_x$.

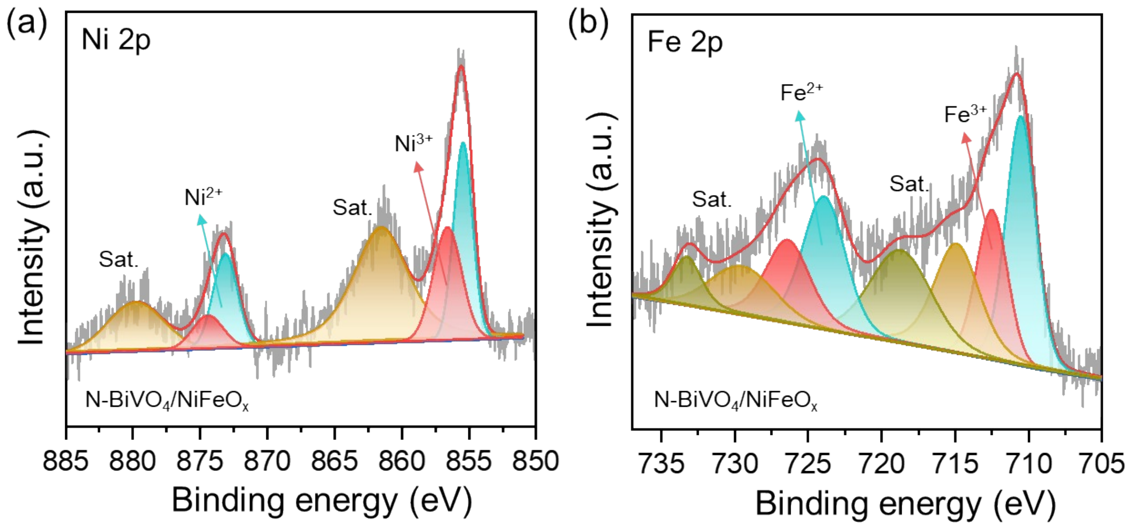

Fig. S8. High-resolution XPS spectra of N-$BiVO_4$/$NiFeO_x$: (a) Ni 2p; (b) Fe 2p.

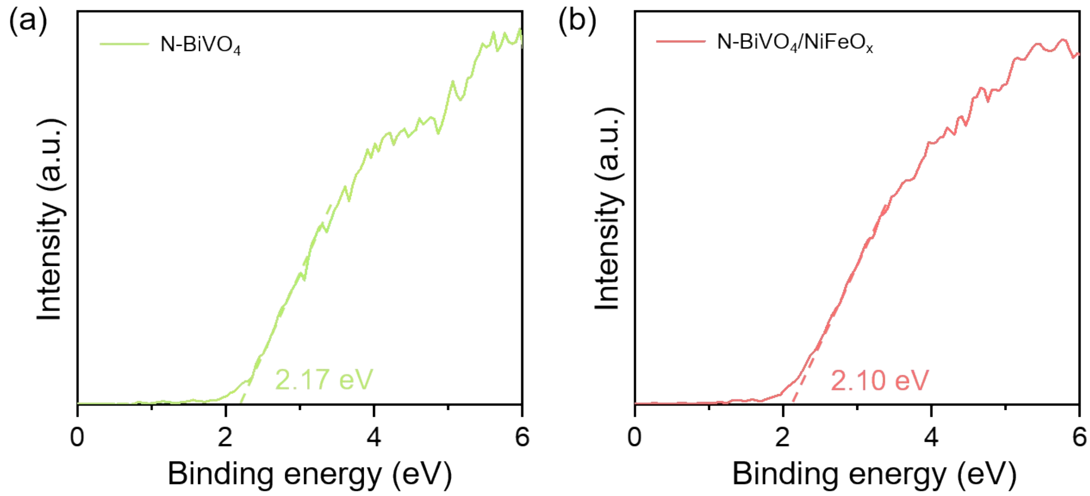

Fig. S9. VB XPS of N-$BiVO_4$ and N-$BiVO_4$/$NiFeO_x$.

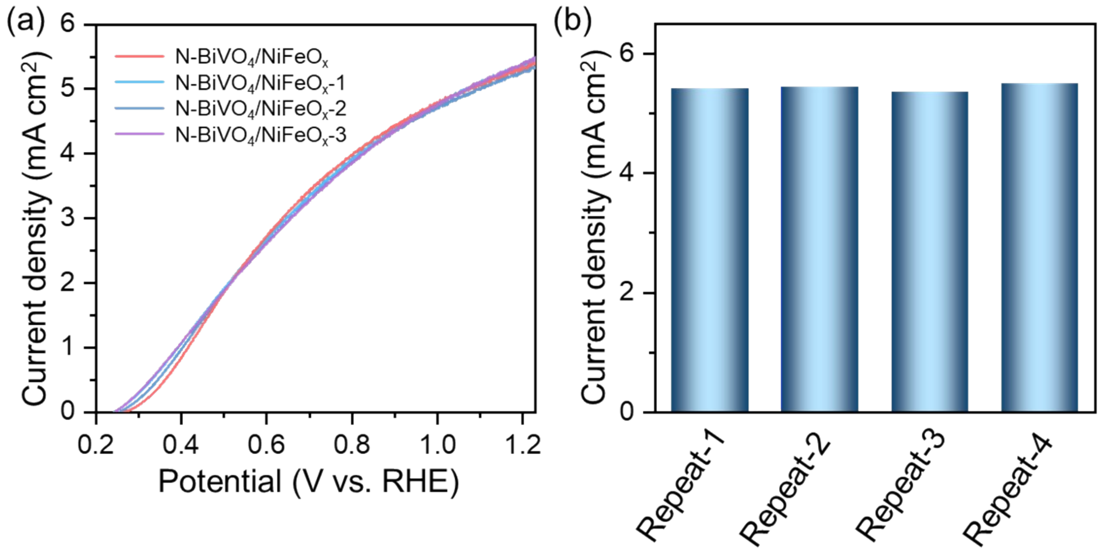

Fig. S10. The repeatability of LSV curves for N-$BiVO_4$/$NiFeO_x$ photoanodes measured in 0.5 M KBi electrolyte.

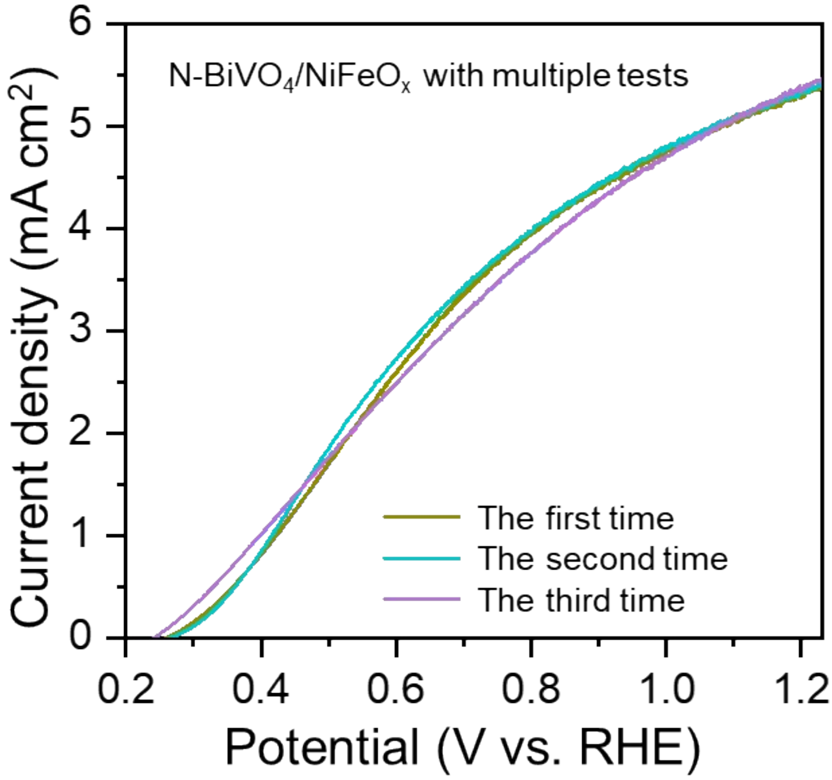

Fig. S11. The multiple test LSV curves for N-$BiVO_4$/$NiFeO_x$ photoanodes measured in 0.5 M KBi electrolyte.

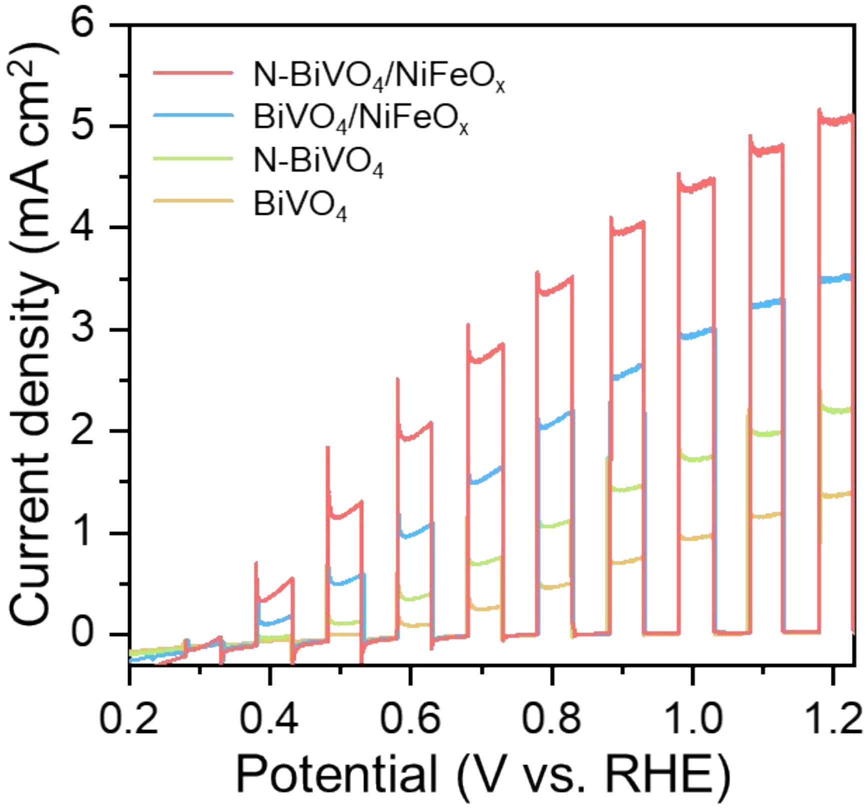

Fig. S12. Chopped photocurrent density in 0.5 M KBi electrolyte (pH=9.3).

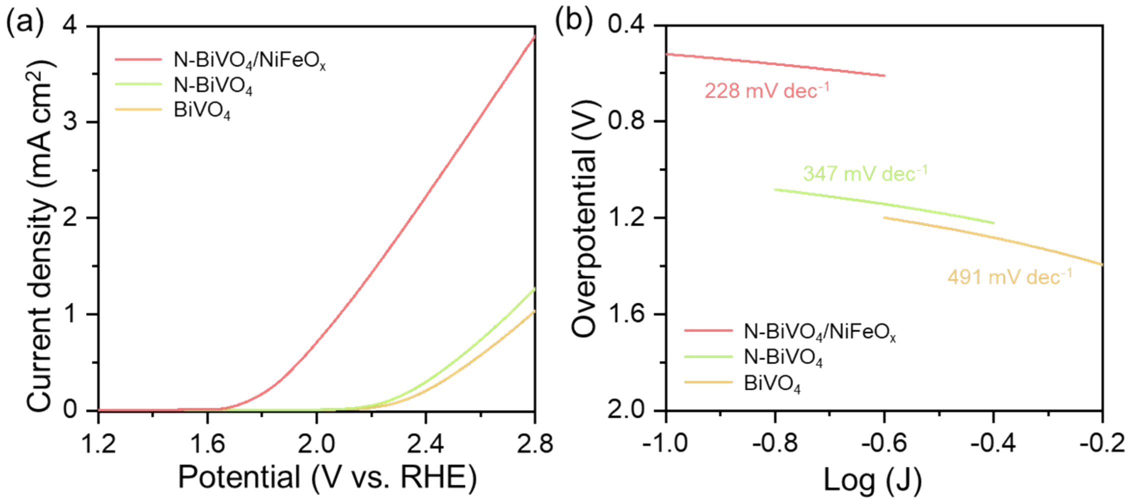

Fig. S13. (a)LSV curves in dark for $BiVO_4$, N-$BiVO_4$ and N-$BiVO_4$/$NiFeO_x$; (b) the estimated Tafel slope for $BiVO_4$, N-$BiVO_4$ and N-$BiVO_4$/$NiFeO_x$.

Fig. S8a shows that the N-$BiVO_4$/$NiFeO_x$ photoanode possesses a lower overpotential and steeper current density, indicating its outstanding electrochemical performance.

In Fig. S8b, the estimated Tafel slope for N-$BiVO_4$/$NiFeO_x$ (228 mV dec^{-1}) is small than that of N-$BiVO_4$ (347 mV dec^{-1}) and $BiVO_4$ (491 mV dec^{-1}), indicating that an enhanced oxygen evolution kinetics.

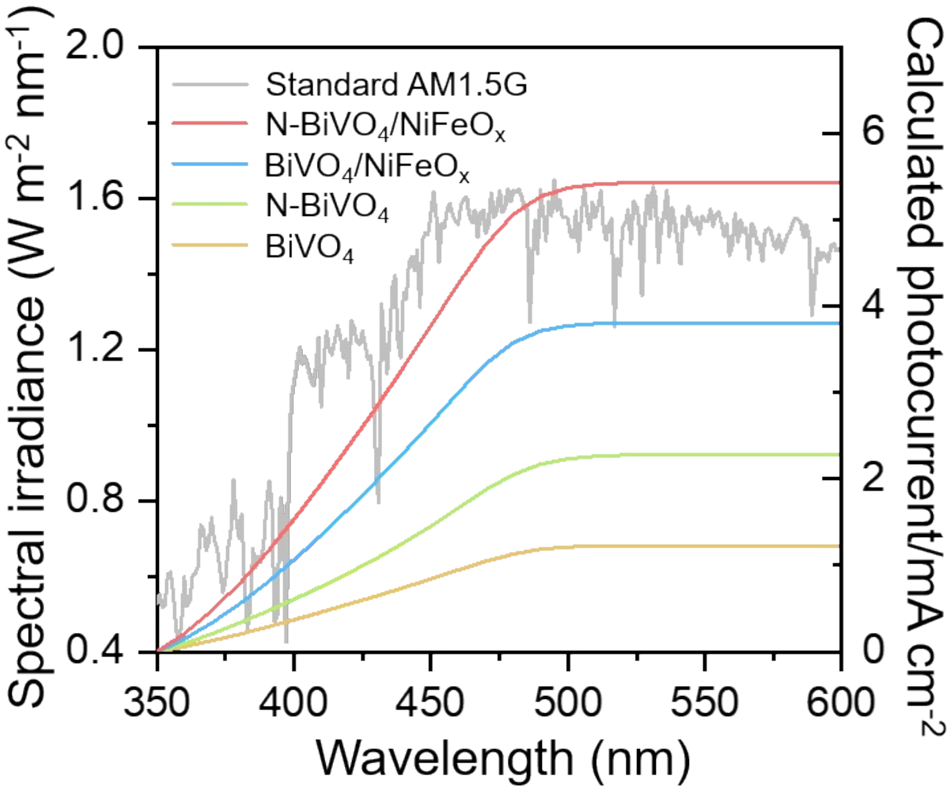

Fig. S14. Calculated photocurrent density curves by integrating IPCE curves (Fig. 3c) and the standard AM 1.5G solar spectrum.

The theoretical photocurrent densities (Jc) for synthetic photoanodes by integrating IPCE values and standard AM 1.5G solar spectrum were obtained by the following equation [1]:

$$J_C(mA/cm^2) = \int_{350}^{600} \frac{\lambda(nm) \times IPCE(\lambda) \times P_{light}(mW/cm^2)}{1240} d(\lambda)$$

Where P_{light} and λ were photocurrent density and the corresponding light wavelength, respectively. Therefore, the calculated values of photocurrent density for $BiVO_4$, N-$BiVO_4$, $BiVO_4/NiFeO_x$ and N-$BiVO_4/NiFeO_x$ were 1.23, 2.28, 3.80 and 5.43 mA/cm^2, respectively. According to Fig. 3a, the measured values for $BiVO_4$, N-$BiVO_4$, $BiVO_4/NiFeO_x$ and N-$BiVO_4/NiFeO_x$ were 1.31, 2.37, 3.81, 5.40 mA/cm^2, respectively. The calculated values are very near the measured values, suggesting the simulated solar light was excellently matched with the standard AM 1.5G solar spectrum.

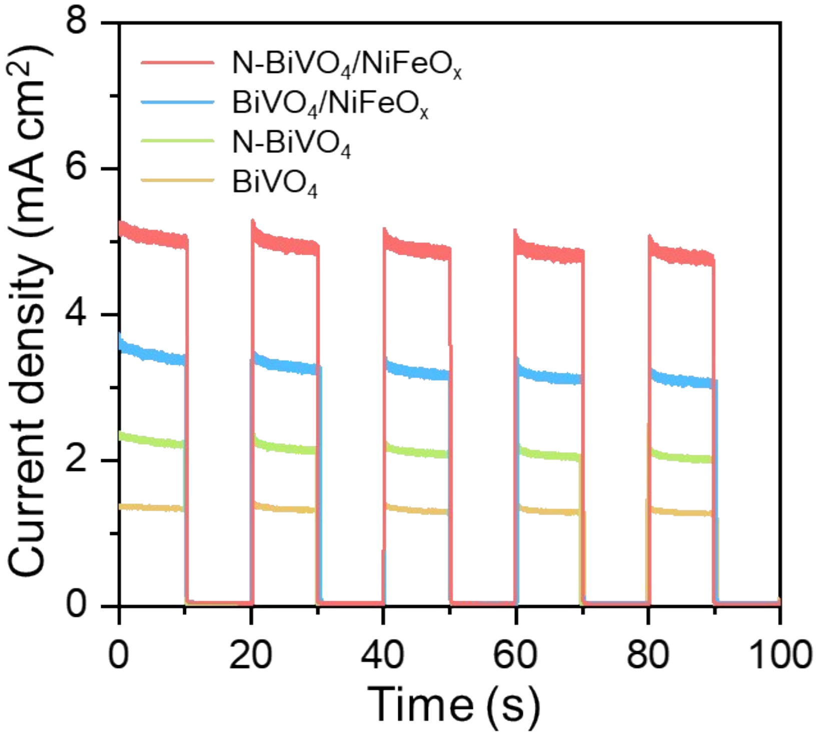

Fig. S15. Photocurrent density under chopping irradiation of $BiVO_4$, N-$BiVO_4$, $BiVO_4$/$NiFeO_x$ and N-$BiVO_4$/$NiFeO_x$ photoanodes.

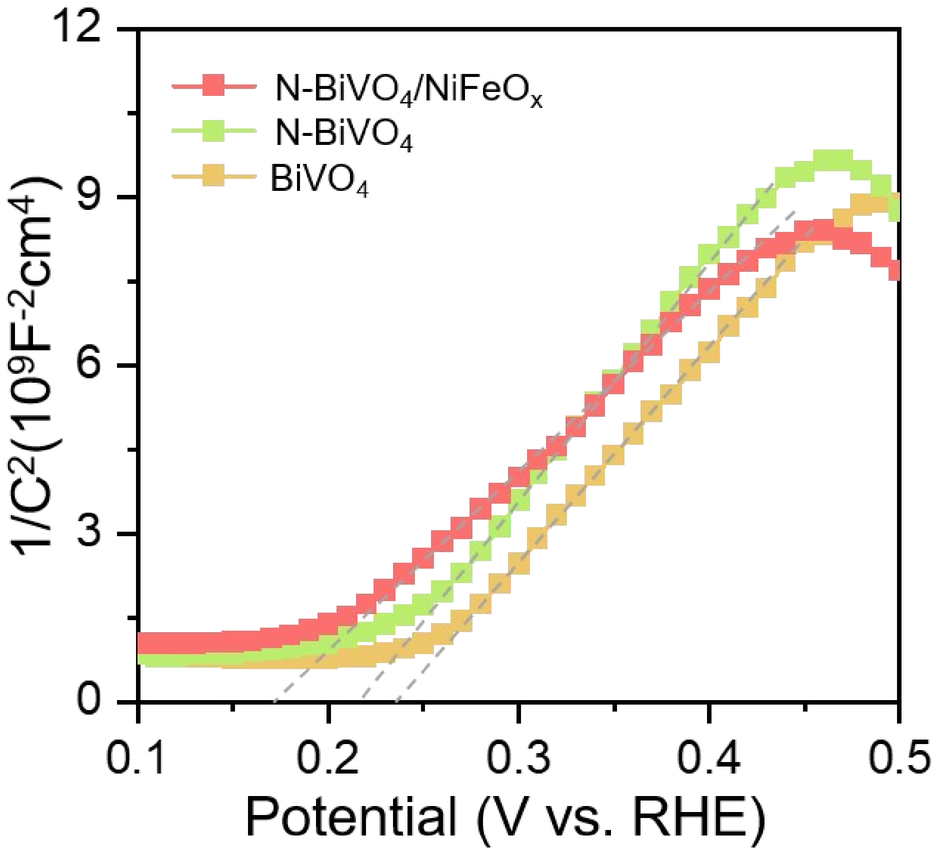

Fig. S16. Mott-Schottky curves under dark of $BiVO_4$, N-$BiVO_4$ and N-$BiVO_4$/$NiFeO_x$.

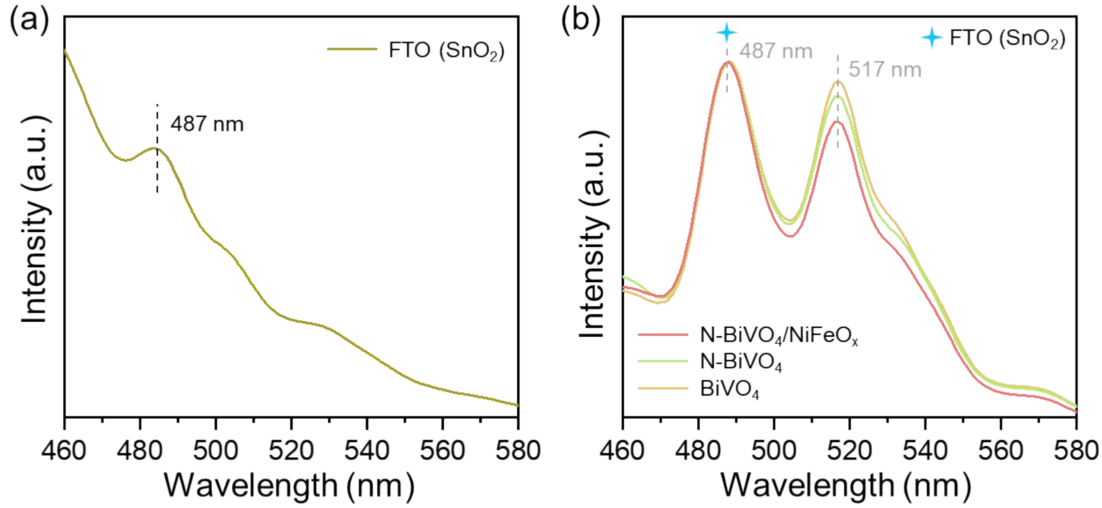

Fig. S17. PL spectrum under laser excitation of 380nm: (a) FTO (SnO_2) substrates; (b) as-prepared photoanodes.

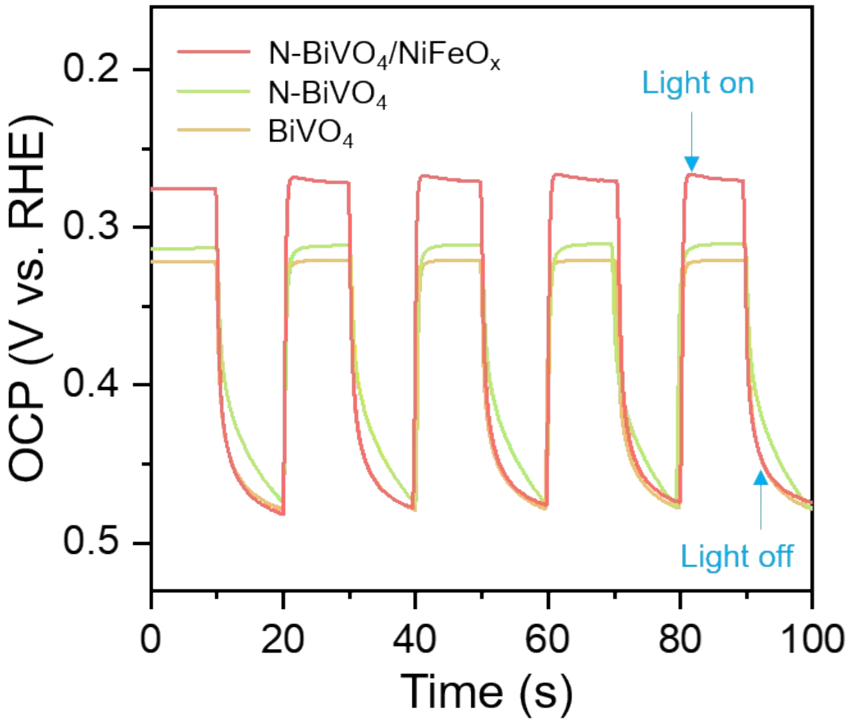

Fig. S18. Open-circuit potential under AM 1.5 G illumination in 0.5 M KBi electrolyte (pH=9.3).

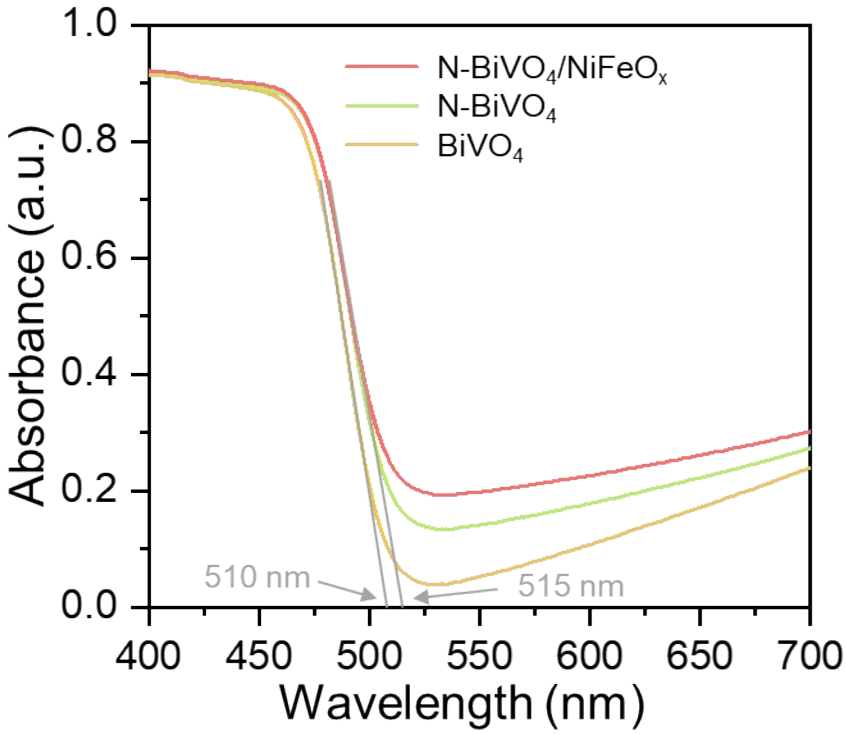

Fig. S19. UV–vis absorbance spectrum of $BiVO_4$, N-$BiVO_4$, and N-$BiVO_4$/$NiFeO_x$ photoanodes.

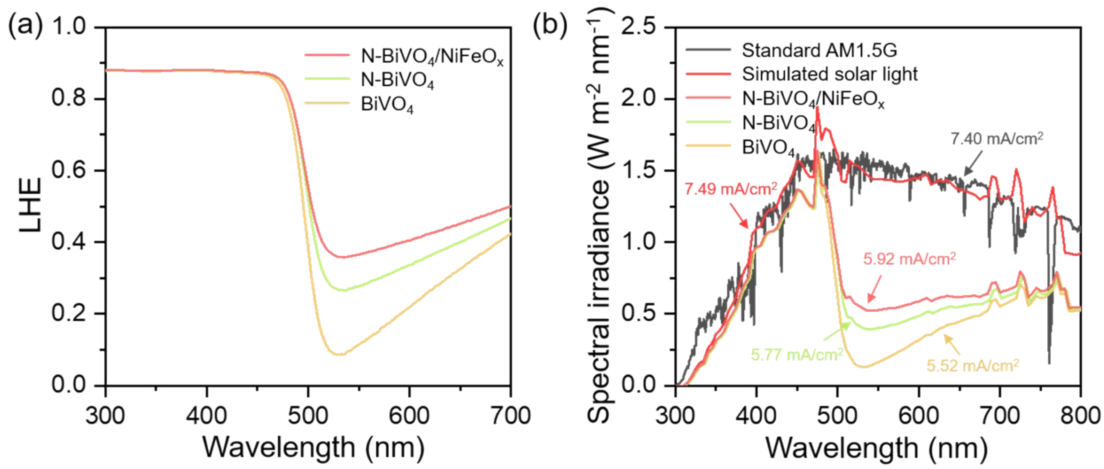

Fig. S20. (a) Light harvesting efficiency (LHE) of $BiVO_4$, N-$BiVO_4$ and N-$BiVO_4$/$NiFeO_x$ photoanodes. (b) Spectra of the simulated solar light and corresponding J_{abs}.

LHE and J_{abs} could be calculated by the following equation [2]:

$$LHE = 1 - 10^{-A(\lambda)}$$

$$J_{abs} = J_{max} \times LHE$$

Where $A(\lambda)$ is absorbance at λ wavelength (nm). J_{max} is the maximum theoretical photocurrent ($mA \cdot cm^{-2}$) under the irradiation of simulated sunlight, and J_{abs} refers to photocurrent ($mA \cdot cm^{-2}$) when light harvesting efficiency is 100%.

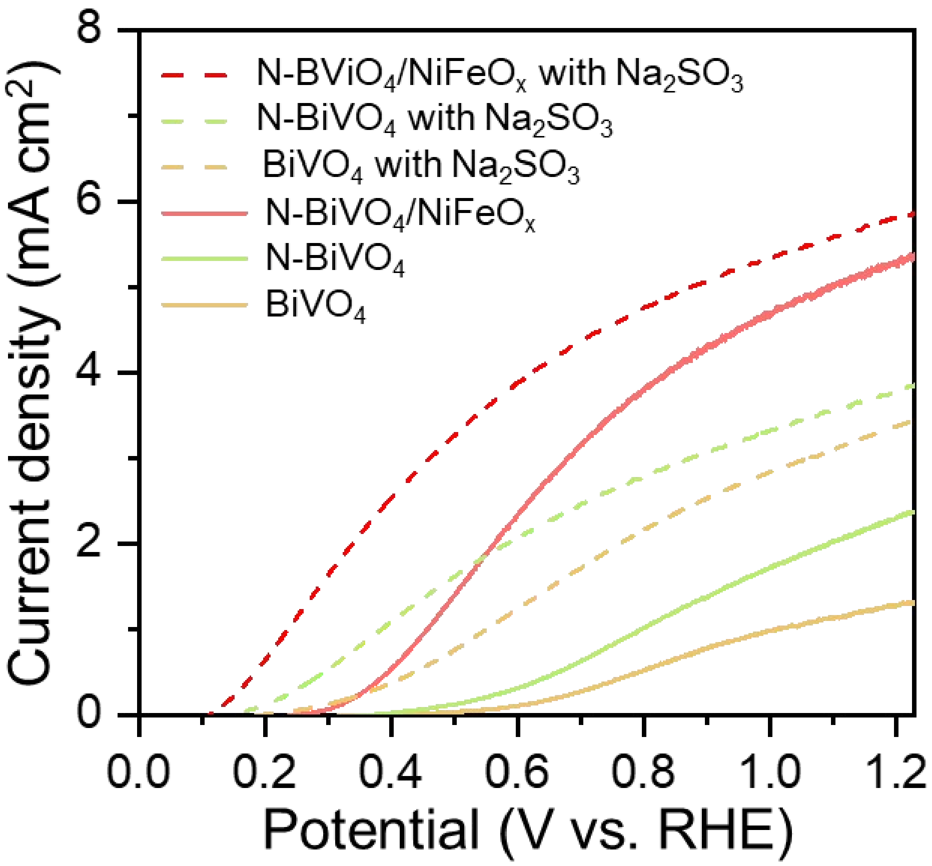

Fig. S21. LSV curves of $BiVO_4$, N-$BiVO_4$ and N-$BiVO_4$/$NiFeO_x$ photoanodes in 0.5 M KBi electrolyte with and without hole scavenger (0.5 M Na_2SO_3).

The charge separation (η_{sep}) and charge transfer efficiencies (η_{tran}) were calculated by the following equation [3]:

$$\eta_{sep} = J_{HS}/J_{abs}$$

$$\eta_{tran} = J_{Ph}/J_{HS}$$

Where J_{HS} refer to photocurrent density (mA·cm^{-2}) measured in KBi containing hole scavenger electrolyte and J_{Ph} is photocurrent density (mA·cm^{-2}) performed in KBi electrolyte.

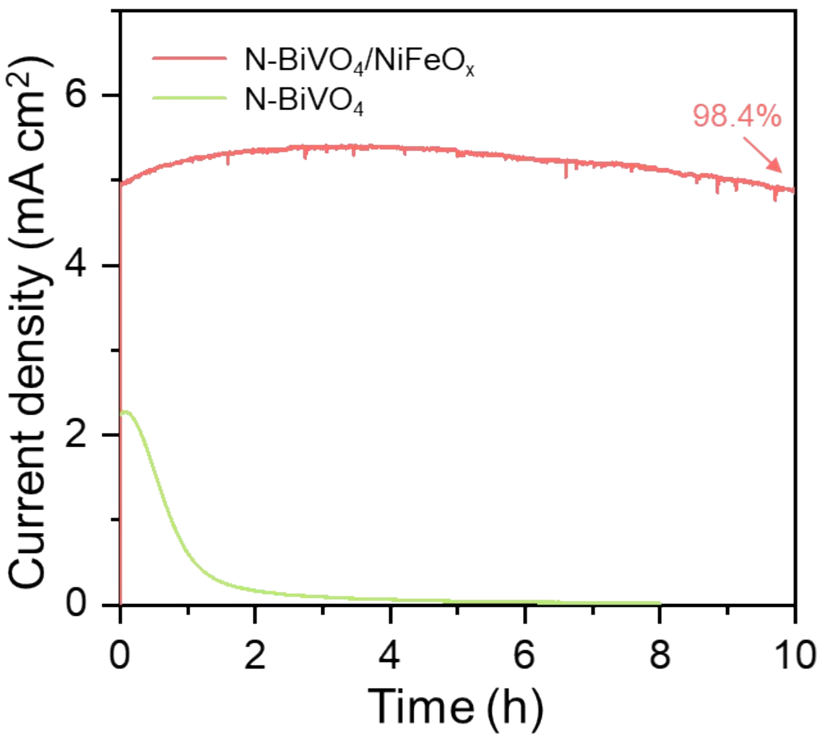

Fig. S22. Photocurrent density stabilities of N-$BiVO_4$/$NiFeO_x$ and N-$BiVO_4$ photoanodes measured in 0.5 M KBi electrolyte at 1.23 V vs. RHE.

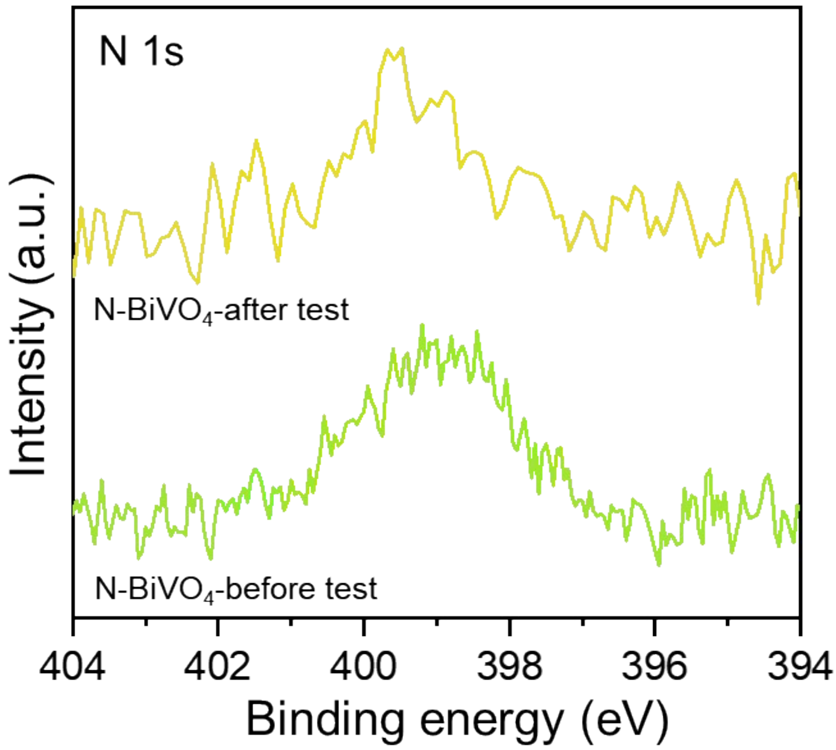

Fig. S23. High-resolution XPS spectra of N 1s for N-$BiVO_4$ before and after test.

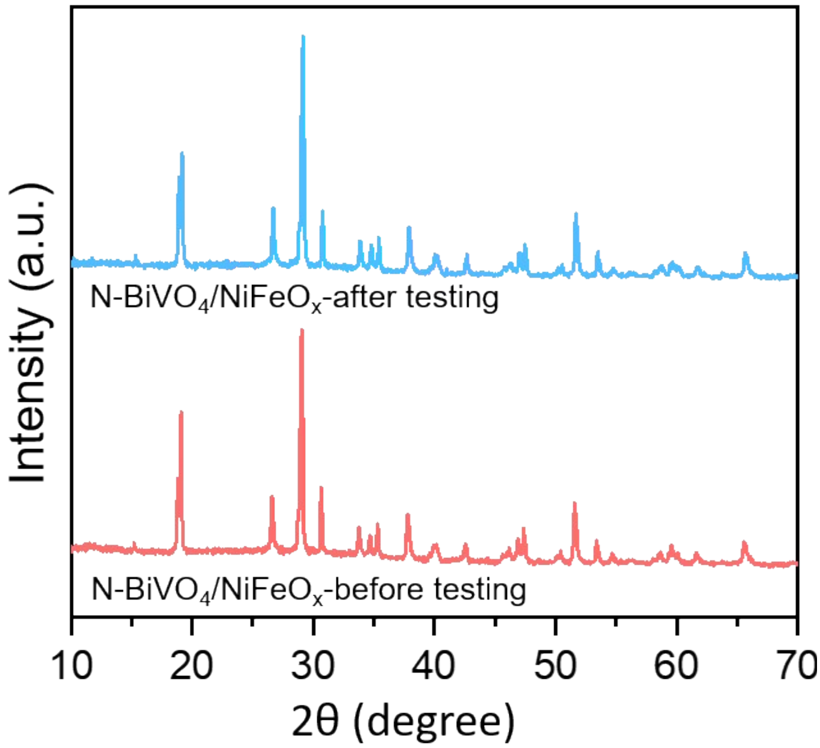

Fig. S24. XRD patterns of N-$BiVO_4$/$NiFeO_x$ photoanode before and after stability testing.

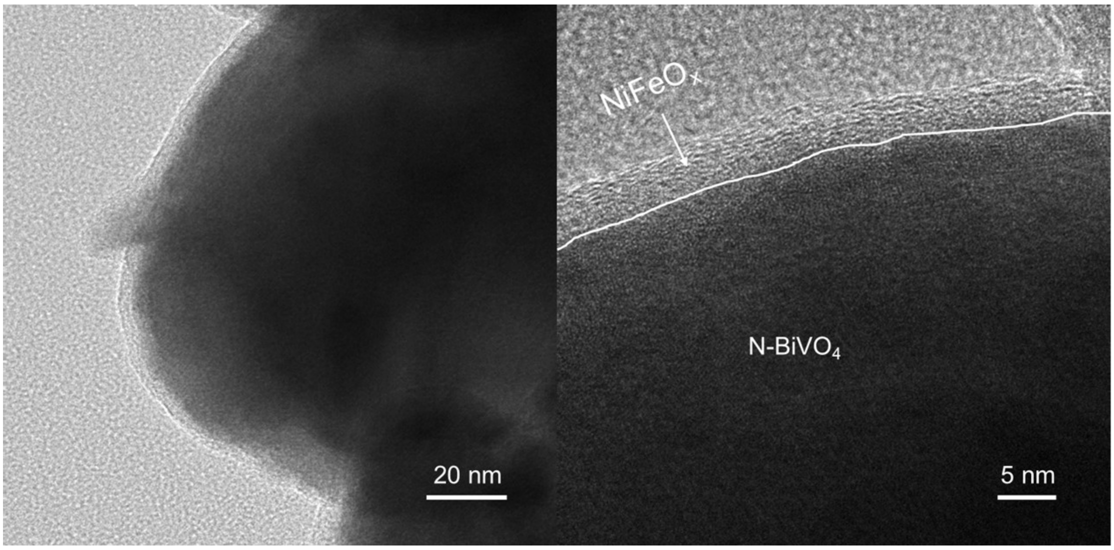

Fig. S22. TEM images of N-$BiVO_4$/$NiFeO_x$ photoanode after stability test.

The HR-TEM image of N-$BiVO_4$/$NiFeO_x$ exhibits that the thickness of $NiFeO_x$ co-catalyst layer is about 4 nm and uniformly decorated on the N-$BiVO_4$ surface.

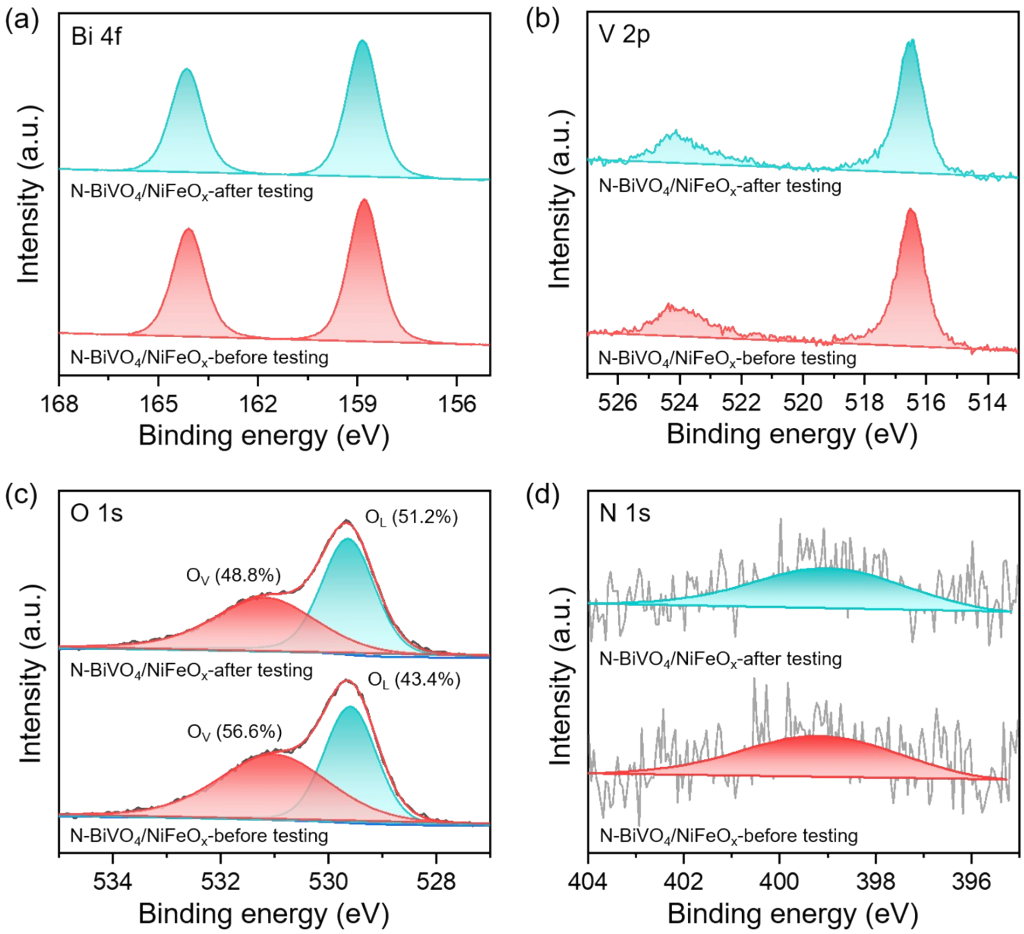

Fig. S23. XPS spectra of N-$BiVO_4$/$NiFeO_x$ photoanode before and after PEC measurements (a) Bi 4f; (b) V 2p; (c) O 1s and (d) N 1s.

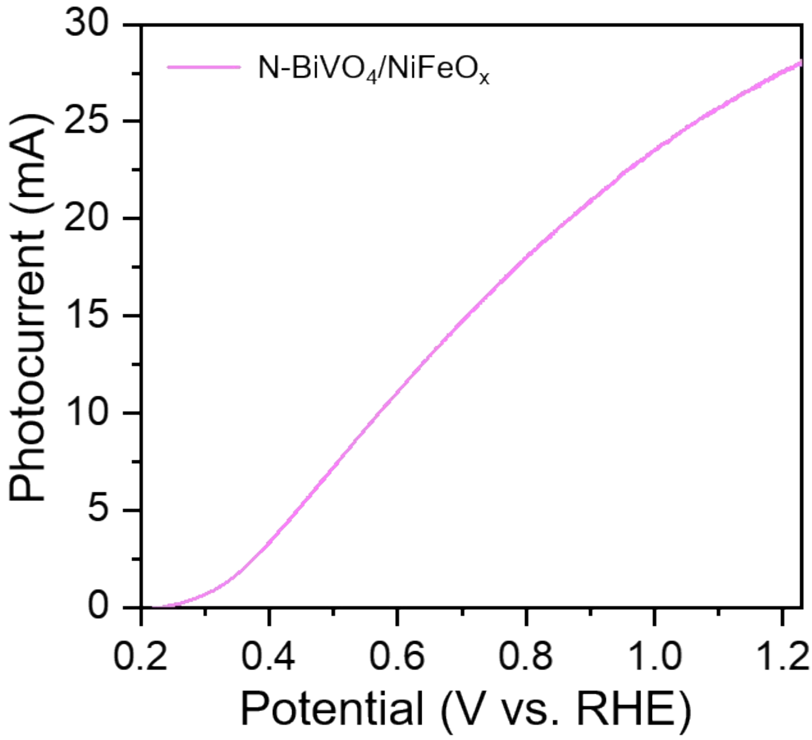

Fig. S24. LSV curve of large size N-$BiVO_4$/$NiFeO_x$ photoanode (9 cm^2).

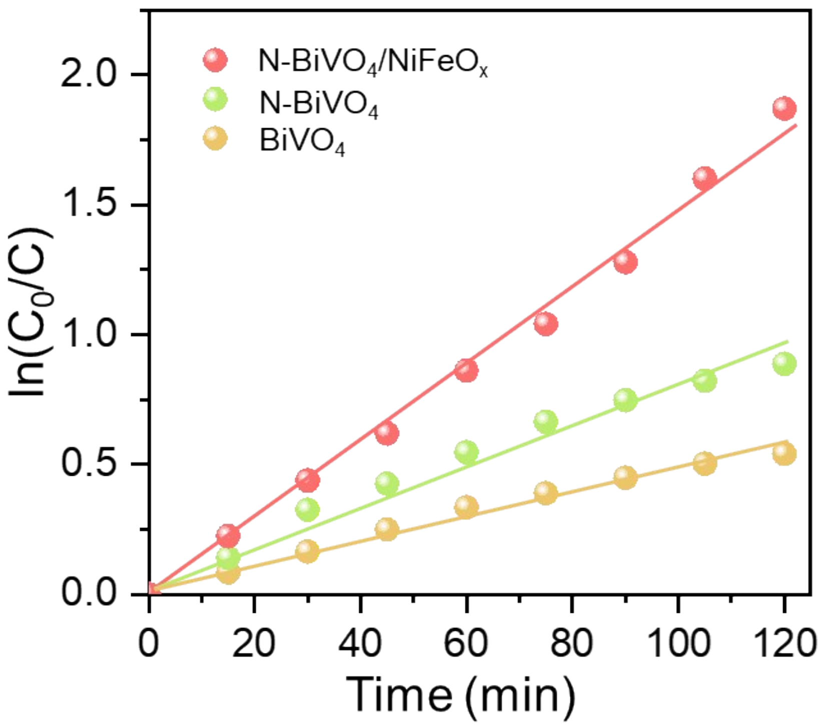

Fig. S25. Comparison of PEC kinetic curves of TCH removal by different photoanodes.

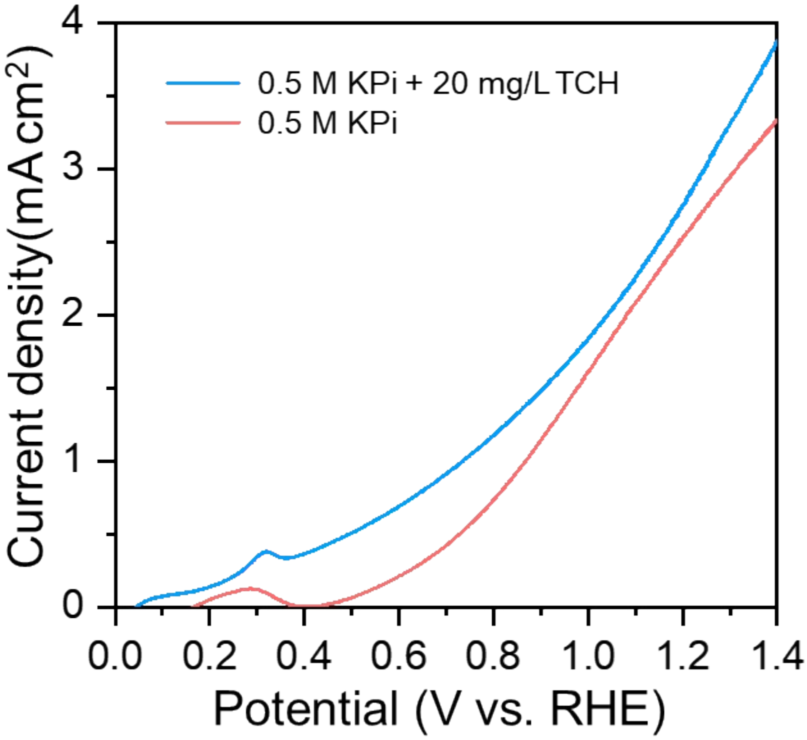

Fig. S26. LSV curves of N-$BiVO_4$/$NiFeO_x$ photoanode measured in different electrolytes.

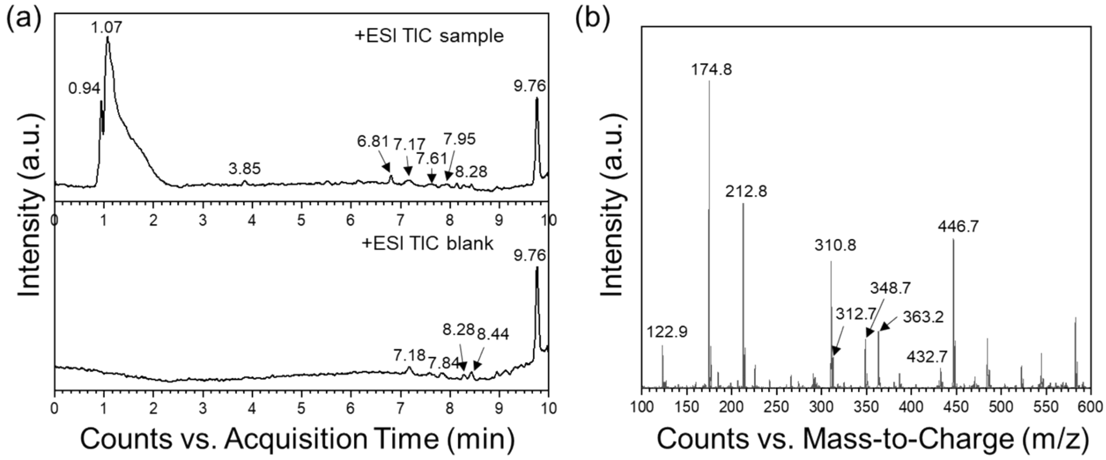

Fig. S27. (a) The LC-MS spectra of the TCH solution during degradation by N-$BiVO_4$/$NiFeO_x$ photoanode; and (b) the total spectrum of mass-to-charge ratio (m/z).

Table S1. The fitted results of EIS curves using the equivalent circuit model in Fig. 3f. (average of three experimental tests).

samples	R_s (Ω)	R_{ct} (Ω)
$BiVO_4$	9.4	137.9
N-$BiVO_4$	8.8	109.2
$BiVO_4$/$NiFeO_x$	9.5	77.4
N-$BiVO_4$/$NiFeO_x$	8.8	46.9

The R_s and R_{ct} refer to solution resistance plus the intrinsic conductivity of samples and charge transfer resistance, respectively [4].

Table S2. Decay-fitted parameters of TRPL decay curves for BiVO4, N-BiVO4 and N-BiVO4/NiFeOx photoanodes.

samples	τ_1 (ns)	τ_2 (ns)	τ_3 (ns)	A_1 (%)	A_2 (%)	A_3 (%)	τ_{avg} (ns)
$BiVO_4$	0.17	0.87	4.40	84.19	12.80	3.01	1.82
N-$BiVO_4$	0.16	1.01	5.16	76.16	20.28	3.56	2.28
N-$BiVO_4$/$NiFeO_x$	0.13	1.35	7.00	89.04	8.61	2.35	3.35

Triple-exponential function fitting was conducted to apply the TRPL decay curves, and the average recombination lifetime (τ_{ave}) was calculated by the equation [5, 6]:

$$L(t) = A_1 e^{-\frac{1}{\tau_1}} + A_2 e^{-\frac{1}{\tau_2}} + A_3 e^{-\frac{1}{\tau_3}} + y_0$$

$$\tau_{avg} = \frac{A_1\tau_1^2 + A_2\tau_2^2 + A_3\tau_3^2}{A_1\tau_1 + A_2\tau_2 + A_3\tau_3}$$

Where τ_1, τ_2 and τ_3 refer to the time constant of the decay processes, and A_1, A_2 and A_3 are their corresponding weighted amplitudes, respectively.

Table S3. Comparison of OER performance for $BiVO_4$ based photoanodes.

Photoanodes	Photocurrent density (1.23 V vs. RHE)	Ref.
$Bi_{1-x}VO_4$/CO-Bi	4.5 mA/cm^2	S7
$BiVO_4$/FeOOH/NiOOH	4.2 mA/cm^2	S8
$BiVO_4$/Co-Sil	5.0 mA/cm^2	S9
β-FeOOH-B- $BiVO_4$	4.96 mA/cm^2	S10
NiOOH/BP/$BiVO_4$	4.48 mA/cm^2	S11
$BiVO_4$/ZnCoFe-LDH	3.43 mA/cm^2	S12
CoNi-MOFs/ $BiVO_4$	3.2 mA/cm^2	S13
Mo:$BiVO_4$@TANF	5.10 mA/cm^2	S14
$BiVO_4$/FeOOH/TANi	4.6 mA/cm^2	S15
H-CoAl-LDH/$BiVO_4$	3.5 mA/cm^2	S16
NiFe-MOFs/ $BiVO_4$	4.61 mA/cm^2	S17
$BiVO_4$/Co_3O_4/CoFe-LDH	3.9 mA/cm^2	S18
$BiVO_4$-N/C-CoPOM	3.3 mA/cm^2	S19
N-$BiVO_4$/$NiFeO_x$	5.40 ± 0.1 mA/cm^2	This work

Table S4. The elemental composition analysis from XPS for N-$BiVO_4$/$NiFeO_x$ photoanode before and after testing.

Element	Atomic % (before testing)	The proportion of relative to C 1s (before testing)	Atomic % (after testing)	The proportion of relative to C 1s (after testing)
C 1s	32.79	100%	37.66	100%
Bi 4f	7.29	22.23%	6.05	16.06%
V 2p	14.97	45.65%	14.27	37.89%
O 1s	36.13	110.19%	34.76	92.30%
N 1s	1.93	5.89%	1.92	5.10%
Ni 2p	2.68	8.17%	1.58	4.20%
Fe 2p	4.2	12.81%	3.75	9.96%

References

[1] B. Zhang, S. Yu, Y. Dai, X. Huang, L. Chou, G. Lu, G. Dong, Y. Bi, Nitrogen-incorporation activates $NiFeO_x$ catalysts for efficiently boosting oxygen evolution activity and stability of $BiVO_4$ photoanodes, Nat. Commun., 2021, **12**, 6969.

[2] Y. Yang, S. Wan, R. Wang, M. Ou, X. Fan, Q. Zhong, NiFe-bimetal-organic framework grafting oxygen-vacancy-rich $BiVO_4$ photoanode for highly efficient solar-driven water splitting, J. Colloid Interface Sci., 2022, **629**, 487-495.

[3] S. Jin, X. Ma, J. Pan, C. Zhu, S.E. Saji, J. Hu, X. Xu, L. Sun, Z. Yin, Oxygen vacancies activating surface reactivity to favor charge separation and transfer in nanoporous BiVO4 photoanodes, Appl. Catal. B: Environ., 2021, **281**, 119477.

[4] T. Pajkossy, R. Jurczakowski, Electrochemical impedance spectroscopy in interfacial studies, Curr. Opin. Electrochem., 2017, **1**, 53-58.

[5] J. Chen, C. Zhang, X. Liu, L. Peng, J. Lin, X. Chen, Carrier dynamic process in all-inorganic halide perovskites explored by photoluminescence spectra, Photonics Res., 2021, **9**, 151-170.

[6] L. Tang, R. Ji, X. Li, K.S. Teng, S.P. Lau, Energy-level structure of nitrogen-doped graphene quantum dots, J. Mater. Chem. C, 2013, **1**, 4908-4915.

[7] Y. Lu, Y. Yang, X. Fan, Y. Li, D. Zhou, B. Cai, L. Wang, K. Fan, K. Zhang, Boosting Charge Transport in $BiVO_4$ Photoanode for Solar Water Oxidation, Adv. Mater., 2022, **34**, 2108178.

[8] W. Kim Tae, K.S. Choi, Nanoporous $BiVO_4$ Photoanodes with Dual-Layer Oxygen Evolution Catalysts for Solar Water Splitting, Science, 2014, **343**, 990-994.

[9] Q. Sun, T. Cheng, Z. Liu, L. Qi, A cobalt silicate modified $BiVO_4$ photoanode for efficient solar water oxidation, Appl. Catal. B: Environ., 2020, **277**, 119189.

[10] Z. Kang, X. Lv, Z. Sun, S. Wang, Y.-Z. Zheng, X. Tao, Borate and iron hydroxide co-modified $BiVO_4$ photoanodes for high-performance photoelectrochemical water oxidation, Chem. Eng. J., 2021, **421**, 129819.

[11] K. Zhang, B. Jin, C. Park, Y. Cho, X. Song, X. Shi, S. Zhang, W. Kim, H. Zeng, J.H. Park, Black phosphorene as a hole extraction layer boosting solar water splitting of oxygen evolution catalysts, Nat. Commun., 2019, **10**, 2001.

[12] X. Wen, M. Fan, Q. Zhao, J. Li, G. Liu, Boosting the Photoactivity of $BiVO_4$ Photoanodes by a ZnCoFe-LDH Thin Layer for Water Oxidation, Chem. Asian. J., 2021, **16**, 4095-4102.

[13] S. Zhou, K. Chen, J. Huang, L. Wang, M. Zhang, B. Bai, H. Liu, Q. Wang, Preparation of heterometallic CoNi-MOFs-modified $BiVO_4$: a steady photoanode for improved performance in photoelectrochemical water splitting, Appl. Catal. B: Environ., 2020, **266**, 118513.

[14] Y. Shi, Y. Yu, Y. Yu, Y. Huang, B. Zhao, B. Zhang, Boosting Photoelectrochemical Water Oxidation Activity and Stability of Mo-Doped $BiVO_4$ through the Uniform Assembly Coating of NiFe–Phenolic Networks, ACS Energy Lett., 2018, **3**, 1648-1654.

[15] T. Tian, G. Jiang, Y. Li, W. Xiang, W. Fu, Unveiling the activity and stability of $BiVO_4$ photoanodes with cocatalyst for water oxidation, Renew. Energ., 2022, **199**, 132-139.

[16] P. Yue, H. She, L. Zhang, B. Niu, R. Lian, J. Huang, L. Wang, Q. Wang, Super-hydrophilic CoAl-LDH on $BiVO_4$ for enhanced photoelectrochemical water oxidation activity, Appl. Catal. B: Environ., 2021, **286**, 119875.

[17] Y. Li, Q. Wang, X. Hu, Y. Meng, H. She, L. Wang, J. Huang, G. Zhu, Constructing NiFe-metal-organic frameworks from NiFe-layered double hydroxide as a highly efficient cocatalyst for $BiVO_4$ photoanode PEC water splitting, Chem. Eng. J., 2022, **433**, 133592.

[18] X. Xu, S. Jin, C. Yang, J. Pan, W. Du, J. Hu, H. Zeng, Y. Zhou, Engineering Interfaces to Steer Hole Dynamics of $BiVO_4$ Photoanodes for Solar Water Oxidation, Sol. RRL, 2019, **3**, 1900115.

[19] K. Fan, H. Chen, B. He, J. Yu, Cobalt polyoxometalate on N-doped carbon layer to boost photoelectrochemical water oxidation of $BiVO_4$, Chem. Eng. J., 2020, **392**, 123744.